

Shock-Wave/Boundary-Layer Interactions at Compression Ramps Studied by High-Speed Schlieren

Zhengzhong Sun*

City, University of London, London, England EC1 V 0HB, United Kingdom
and

Tian Gan[†] and Yun Wu[‡]

Xi'an Jiaotong University, 710076 Xi'an, People's Republic of China

<https://doi.org/10.2514/1.J058257>

The shock-wave/boundary-layer interactions (SWBLIs) at compression ramps (ramp angle $\alpha = 20\text{--}30^\circ$) are studied at $Ma = 2.0$ and under two Reynolds numbers ($Re_1 = 18,600$ and $Re_2 = 35,600$, with the Reynolds number Re based on boundary-layer thickness). High-speed schlieren operating at 20 kHz are used as the flow diagnostics. The flow structures in the compression ramp SWBLIs (including the shock wave, interaction region, and induced turbulent region over the ramp surface) are discussed. Their variations under increasing ramp angles and Reynolds numbers are further examined. The low-frequency shock-wave oscillations are also studied through tracking the shock-wave motion. A larger ramp angle increases the spectral intensity of the shock wave's low-frequency unsteadiness, whereas increasing the Reynolds number results in a lower peak frequency for the separation and reattachment shock waves.

Nomenclature

f	=	frequency
h	=	ramp height
I	=	schlieren intensity
L	=	length of interaction region
l	=	the length of model top surface upstream of the ramp
Ma	=	Mach number
N	=	number of images
P	=	spectrum magnitude
Re	=	Reynolds number
St	=	Strouhal number
U_∞	=	freestream velocity
x	=	the streamwise coordinate
y	=	the wall-normal coordinate
α	=	ramp angle
δ	=	boundary-layer thickness
ϵ	=	residual

Subscripts

i	=	interaction
L	=	length of interaction region
mean	=	mean flow quantity
RMS	=	root mean square
s	=	separation
1, 2	=	Reynolds numbers 1 and 2
θ	=	boundary-layer momentum thickness

I. Introduction

THE shock-wave/boundary-layer interaction (SWBLI) is a critical phenomenon in transonic and supersonic aerodynamics. The occurrence of a SWBLI gives rise to unsteady flow separation and enhanced turbulence intensity, which induces drag and affects aerodynamic efficiency. As the SWBLI underpins many transonic and supersonic applications, a lot of research efforts have been attracted for more than half a century [1]. The SWBLIs at the compression ramp [2] and those induced by an oblique incident oblique shock wave [3] are widely adopted as the baseline cases, and in-depth fundamental understandings have been generated. These two types of SWBLIs also represent simplified geometries encountered in practical aerodynamic applications, such as the supersonic inlet [4,5]. The present research chooses to examine the SWBLI established at a compression ramp.

The compression ramp induced SWBLI has been studied through experimental and numerical methods under different Mach numbers and Reynolds numbers. A comprehensive summary is provided in the monograph dedicated to SWBLI [6]. Knowledge on the overall flow structure has been well established. The major flow features include the separation and reattachment shock waves, the interaction region, and the boundary-layer separation and reattachment. The length of the interaction region is one important parameter. Its growth with increasing ramp angle has been studied through a series of experiments at $Ma = 3.0$ by Zheltovodov [7]. This research was thereafter used as the benchmark case for simulation validation [2,8,9]. In the direct numerical simulation (DNS) study of a 24 deg compression ramp at $Ma = 2.9$ [2], the leading edge of the time-averaged interaction region extended to $x_s/\delta = -2.1$, where the origin of the x axis was at the ramp foot. Another large-eddy simulation (LES) on a 25 deg compression ramp at $Ma = 2.88$ revealed that the interaction started from $x_s/\delta = -4.0$ [8], which is nearly doubled from that in Ref. [2]. The different interaction length is likely a result of the Reynolds number effect because the two SWBLIs were simulated under $Re_\theta = 2900$ and 5385, respectively. Therefore, a larger Reynolds number produces a longer nondimensional interaction region. A more recent DNS study on a 25 deg ramp at $Ma = 2.9$ and $Re_\theta = 2372$ revealed a separation length of $x_s/\delta = -2.44$ [9], which confirmed the Reynolds number effect because it was close to that in Ref. [7]. Reviewing the literature on supersonic compression ramps, most of the works have Mach numbers around 3.0. In contrast, studies on a lower Mach number, such as $Ma = 2.0$, are less systematic. Moreover, a lower Mach number of around 2.0 is relevant to the commercial supersonic transportation that is currently being reinvestigated. Hence, the present experiment aims to analyze

Received 2 January 2019; revision received 14 October 2019; accepted for publication 16 October 2019; published online Open Access 26 November 2019. Copyright © 2019 by Zhengzhong Sun, Tian Gan, and Yun Wu. Published by the American Institute of Aeronautics and Astronautics, Inc., with permission. All requests for copying and permission to reprint should be submitted to CCC at www.copyright.com; employ the eISSN 1533-385X to initiate your request. See also AIAA Rights and Permissions www.aiaa.org/randp.

*Senior Lecturer, Department of Mechanical Engineering and Aeronautics, Northampton Square.

[†]Lecturer, Department of Mechanical Engineering, 28 Xianning West Road.

[‡]Professor, Department of Mechanical Engineering, 28 Xianning West Road; wuyun1223@126.com (Corresponding Author).

Table 1 Flow and model parameters

Parameter	Quantity
Mach number	$Ma = 2.0$
Freestream velocity	$U_\infty = 514 \pm 5$ m/s
Ramp height	$h = 20$ mm
Ramp angle	$\alpha = 20, 22, 24, 26, 28, 30$ deg
Streamwise length for boundary-layer development	$l_1 = 150$ mm $l_2 = 360$ mm
Boundary-layer thickness	$\delta_1 = 2.3$ mm $\delta_2 = 4.4$ mm
Reynolds number (based on δ)	$Re_1 = 18,600$ $Re_2 = 35,600$

SWBLIs at compression ramps under $Ma = 2.0$ flow. At the same time, the Reynolds number effect will also be examined.

The interaction region features low-frequency unsteadiness in the SWBLI, which is two magnitudes smaller than that in the incoming turbulent boundary layer [10]. Studies have been directed to explore the origin of the low-frequency unsteadiness so that an appropriate flow control method can be designed. The upstream and downstream sources of the low-frequency unsteadiness have been identified and summarized in a review paper [11]. The surface pressure sampled at a fast recording rate was used to reveal the unsteadiness in SWBLIs. In the work of Dupont et al. [10] on an incident shock SWBLI, the low-frequency shock oscillation had $St_L = 0.02$ – 0.05 , where St_L is the Strouhal number based on interaction length. Priebe and Pino Martin [2] found that the power spectrum of the fluctuating pressure inside the interaction region was broadband in general. In particular, the spectrum at the shock-wave location had an intensified energy in the band of $St_\delta = 0.002$ – 0.03 (peak magnitude at $St_\delta = 0.01$), whereas the pressure power spectra within the interaction region exhibited enhanced energy in a higher band of $St_\delta = 0.04$ – 5 . Grilli et al. [12] reported an even lower peak frequency for the shock oscillation (namely, $St_\delta = 0.004$), whereas the wall pressure power spectra at locations inside the separation region shifted toward higher Strouhal numbers, which were still smaller than those in the incoming boundary layer. Another objective of the present study is to reveal the shock-wave unsteadiness: especially the modulation of shock-wave spectrum under the influence of the ramp angle and Reynolds number. Instead of measuring the instantaneous wall pressure, the temporal motion of the shock wave is tracked through schlieren images recorded at a high sampling rate; namely, the schlieren is used as an optical sensor.

In summary, the present experimental research on compression ramp SWBLIs is conducted to study the Reynolds number effect on the SWBLI structure, as well as the shock-wave unsteadiness. Six ramps with angles ranging from 20 to 30 deg with an interval of 2 deg are measured so that the effect of the ramp angle or interaction strength can also be revealed. High-speed schlieren operating at 20 kHz is used as the flow instrumentation. In the remainder of the paper, the experimental setup is first introduced, followed by the detailed discussions on the experimental results reflecting the ramp angle effect and the Reynolds number effect. Conclusions are finally drawn at the end of the paper.

II. Experimental Setup

A. Wind-Tunnel and Test Models

The supersonic wind tunnel at Xi'an Jiaotong University is used as the flow facility. This wind tunnel is a suction-type facility. The flow is driven by the pressure difference between the ambient and the vacuum downstream of the diffuser. The total pressure and total temperature are 1 atm and 300 K, respectively. In the experiment, a Mach 2.0 nozzle is used. Before the nozzle inlet, a cluster of 18 fine-mesh screens is used to straighten the flow and reduce turbulence. The nozzle outlet has a diameter of 300 mm, and the supersonic free jet enters a cylindrical test chamber with a diameter of 1.5 m, which is made big enough to eliminate wall interference toward the supersonic flow. The test chamber connects to a 120 m³ vacuum tank through a diffuser.

The Perspex test model comprised two parts: the base plate with a flat top surface, and the ramp piece. Two base plates with different lengths are available. The longer plate allows further development of the turbulent boundary layer, resulting in a larger boundary-layer thickness. Both plates have the same width of $w = 110$ mm. Six ramp pieces are going to be tested; their angles are $\alpha = 20$ – 30 deg with an interval of 2 deg. All the ramp pieces have the same height of $h = 20$ mm and are topped by a flat surface. The ramp is installed $l_1 = 150$ mm from the leading edge on the shorter plate, whereas it is $l_2 = 360$ mm on the longer plate. The compression ramp model is sketched in Fig. 1a. The boundary layer at the location of the ramp is found to have thicknesses of 2.3 and 4.4 mm for the two models, respectively, through schlieren visualization. A separate particle image velocimetry measurement reveal that the freestream velocity is 514 m/s and the turbulence intensity is about 1%. The Reynolds numbers based on boundary-layer thickness are $Re_1 = 18,600$ and $Re_2 = 35,600$, respectively. The model is installed onto the mounting plate at the bottom of the test chamber through a wedge-shaped vertical strut. The installation of the test model is sketched conceptually in Fig. 1b. The relevant flow and model parameters are summarized in Table 1.

B. High-Speed Schlieren

The present schlieren setup follows a Z-type light path. The illumination is provided by a Gloria 500 W xenon lamp. A Phantom V2512 ultra-high-speed camera is used to record the schlieren images. The camera sensor has 1280×800 pixels with a $20 \mu\text{m}$ pixel pitch. The field of view covers an area of 237×148 mm², resulting in a spatial resolution of 0.185 mm/pixel and a magnification factor of 0.11. The acquisition is initiated as soon as the wind-tunnel flow starts. The knife edge is placed vertically; hence, the horizontal density gradient is amplified. The schlieren setup remains the same for both Reynolds number cases. The image acquisition frequency is 20 kHz so that the temporal motion of the shock wave can be resolved. The camera exposure time is set to $1 \mu\text{s}$ to freeze the turbulent structures.

Schlieren technique is mostly used as a qualitative flow visualization technique for the shock wave and other flow structures where a large density gradient is present. With some fine tunings of the schlieren setup, such as reducing the camera exposure time or using a nanosecond pulsed light source (e.g., the spark light

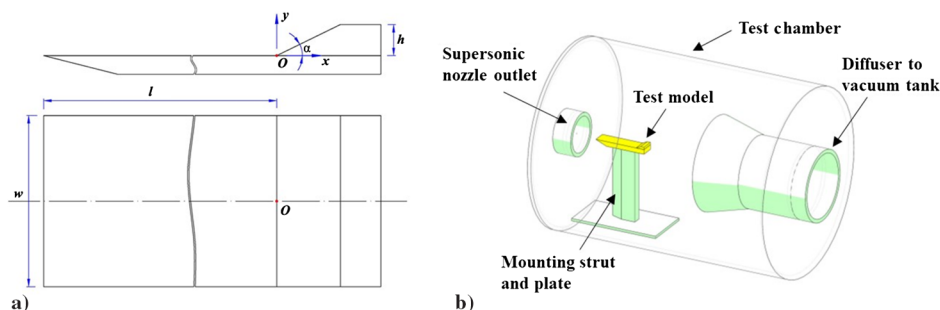


Fig. 1 Compression ramp model a) with coordinate system and b) its installation in the wind tunnel.

and pulsed laser), the flow structures can be captured with sharp edges. For example, a recent schlieren experiment using a pulsed laser successfully visualized the intermittent vortical structure in hypersonic boundary-layer transition [13].

Apart from qualitative observation of the schlieren snapshots, the RMS schlieren intensity field was used as a semiquantitative way to reveal the flowfield fluctuations. A recent experimental study by Combs et al. [14] visualized the amplification of fluctuation intensity in the separation region of transitional SWBLIs under increasing Reynolds numbers. The statistics of the recorded schlieren intensity fields (namely, the mean I_{mean} and the root-mean-square I_{RMS}) are also going to be examined in the present paper. The convergence of the two statistical quantities is enabled by the large image ensemble. For the SWBLIs at Re_1 , the dataset for each ramp case has 10,000 images, whereas there are 9000 images for each case at Re_2 . A residual quantity ε is defined, which is the maximum absolute difference between $I(i, j)_{\text{mean}}^N$ and $I(i, j)_{\text{mean}}^{N-1}$ or between $I(i, j)_{\text{RMS}}^N$ and $I(i, j)_{\text{RMS}}^{N-1}$, namely,

$$\varepsilon_{I_{\text{mean}}} = \max(|I(i, j)_{\text{mean}}^N - I(i, j)_{\text{mean}}^{N-1}|)$$

$$\varepsilon_{I_{\text{RMS}}} = \max(|I(i, j)_{\text{RMS}}^N - I(i, j)_{\text{RMS}}^{N-1}|)$$

where $I(i, j)_{\text{mean}}^N$ is the mean schlieren intensity field based on a number of N images, and (i, j) are the i th and j th pixels along the horizontal and vertical directions, respectively. The evolutions of $\varepsilon_{I_{\text{mean}}}$ and $\varepsilon_{I_{\text{RMS}}}$ with the number of images N for the 30 deg ramp case at Re_1 and Re_2 are shown in Fig. 2. The largest ramp is chosen

because the induced SWBLI produces strong turbulence over the ramp surface, which normally requires a larger ensemble to achieve convergence. According to Fig. 2, $\varepsilon_{I_{\text{mean}}}$ converges to a smaller magnitude than $\varepsilon_{I_{\text{RMS}}}$, whereas $\varepsilon_{I_{\text{mean}}}$ also has narrower scattering. Despite the differences, residuals for both I_{mean} and I_{RMS} are close to 0.01 counts when the full range of images are used, which corresponds to about 0.5% of the RMS schlieren intensity in the freestream region. For the purpose of clarity, the convergence curves for the other SWBLI cases are not shown, but they have similar features; their final residuals are also close to 0.01 counts. Convergence can therefore be concluded for I_{mean} and I_{RMS} .

III. Results and Analysis

A. Effect of Ramp Angle

The ramp angle effect is first explored through the SWBLIs at Re_1 . The schlieren snapshots for the six compression ramps are shown together in Fig. 3. It is clear that increasing the ramp angle α gradually moves the separation shock wave upstream. The inviscid shock origination point is at $x/h = -0.6$ in the $\alpha = 20^\circ$ deg SWBLI, and it moves to $x/h = -1.5$ in the $\alpha = 30^\circ$ deg SWBLI, corresponding to a longer interaction zone. Verma et al. [15] reported an experiment on a 24 deg compression ramp SWBLI at $Ma = 2.05$, where the incoming boundary-layer thickness was 3.85 mm. The interaction length of the SWBLI in Ref. [15] was about 20 mm, which is similar to its counterpart in Fig. 3c. The reattachment shock wave gradually builds up strength, following the increase of α . However, it is not as focused as the separation shock wave, even in the 30 deg ramp SWBLI. The turbulent region over the ramp surface also becomes

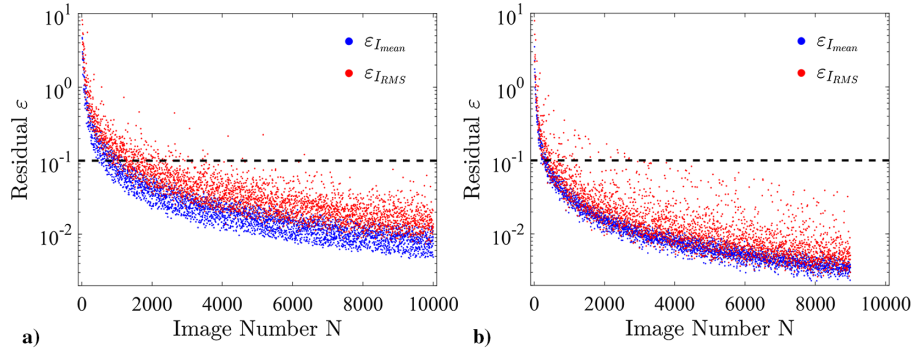


Fig. 2 Evolution of $\varepsilon_{I_{\text{mean}}}$ and $\varepsilon_{I_{\text{RMS}}}$ with the number of images N for the 30 deg ramp SWBLIs at a) Re_1 and b) Re_2 .

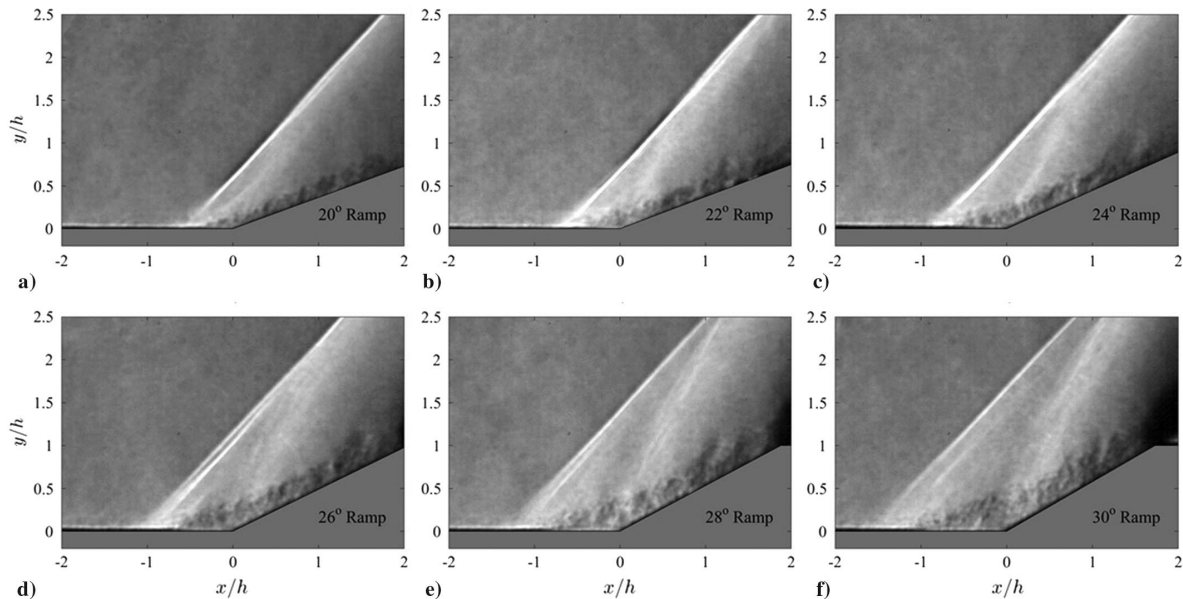


Fig. 3 Schlieren snapshots for SWBLIs at Re_1 .

thicker over a steeper ramp. Its thickness is $0.2h$ over the 20 deg ramp and is thickened to nearly $0.5h$ over the 30 deg ramp. The separation shock waves in all the SWBLIs in Fig. 3 have a similar angle of 47 deg, suggesting that the flow deflection angle due to the ramp is alleviated by the turbulent wedge formed in the interaction zone. The reattachment shock wave can be clearly seen when $\alpha \geq 24$ deg, and it gets stronger over a larger compression ramp. Due to the upstream movement of the separation shock wave, the two shock waves are further separated following the increase of α .

The short camera exposure time allows visualization of some transient flow features (Fig. 3). The alternating bright and dark patterns can be observed in the interaction region and over the ramp, indicating the vortical activity. It will be revealed that all these moving structures contribute to the contoured distribution of the RMS schlieren intensity I_{RMS} .

The I_{RMS} in the SWBLIs at Re_1 were calculated and are shown in Fig. 4. The I_{RMS} contour range is set from 1 to 12 counts, which is chosen to resolve the I_{RMS} distribution in the near-wall turbulent region. Because the I_{RMS} associated with the shock wave is significantly stronger than the other part of the flowfield, the shock waves in Fig. 4 are saturated by the red color. The separation shock wave remains strong for all the cases, except its foot region close to the wall. This “weak” foot region usually comprises compression waves and extends further above the wall for larger ramps. The reattachment shock wave is also represented by the concentration of I_{RMS} . It is clearly visualized in the SWBLIs when $\alpha = 28$ and 30 deg, but it is only partially visualized near the triple point in the SWBLI when $\alpha = 26$ deg.

Due to the interaction of the boundary layer and shock wave, the near-wall region after the separation shock wave has much stronger I_{RMS} than that in the incoming turbulent boundary layer, which agrees with the observation in the raw schlieren snapshots in Fig. 3. Two subdomains can be distinguished: one is the interaction zone, and the other is the turbulent region over the ramp surface. The I_{RMS} in the latter subdomain features a concentric elliptical distribution, where the position of peak I_{RMS} corresponds to the location of peak fluctuation of density gradient, which is likely linked to the strongest vortical event in the shear layer. The peak I_{RMS} magnitude becomes larger, and it moves downstream over a steeper ramp. In the LES of a SWBLI at a 25 deg compression ramp [12], a peak u_{RMS} is revealed over the ramp surface, and an increased level of velocity fluctuation happens along the separated shear layer. Although, the RMS of density variation was not presented in that work, as velocity and density fluctuations are closely correlated in compressible flow, enhanced density fluctuations can be conjectured in the separated shear layer and the turbulent region over the ramp.

Closer inspection on the I_{RMS} contours can detect a small region at the ramp corner, in which the I_{RMS} intensity is distinctively weaker than the surrounding area. Close-up views on this region are provided in Fig. 5. This region of weak I_{RMS} is speculated to be in association with the separation bubble, which has fewer fluctuations than the separated shear layer. In the LES study mentioned earlier [12], the region of the separation bubble was also found of weaker velocity fluctuations than the separated shear layer. However, the relation between the low I_{RMS} region at the corner and the separation bubble still needs validation.

B. Effect of Reynolds Number

To explore the Reynolds number effect, the SWBLIs at Re_2 are examined here. The schlieren snapshots for each case are shown in Fig. 6. The longer plate allows further development of the incoming turbulent boundary layer, resulting in a larger thickness of 4.4 mm at the location of the ramp. The present Reynolds number based on boundary-layer thickness is $Re_2 = 35,600$. It should be mentioned that the schlieren images in Fig. 6 are slightly brighter than those in Fig. 3, despite the schlieren setup remaining unmoved in the experimental campaign. Because the measurements for Re_1 and Re_2 were performed in two consecutive days, the thermal effect and vibration might cause the slight displacement of the cutoff knife.

Comparing the SWBLIs at Re_1 and Re_2 , it can be appreciated that the Reynolds number (or the boundary-layer thickness) underpins the shock-wave structure. The separation shock wave in the 20 deg ramp SWBLI has the inviscid origin at $x = -2h$, resulting in a much longer interaction region than that at Re_1 . Increasing the ramp angle lengthens the interaction region. The growth of L_i with the ramp angle at both Reynolds numbers is shown in Fig. 7. Figure 7a reveals the growth of L_i/h . For the whole range of ramp angles, the L_i at Re_2 is about $1.2h$ longer than that at Re_1 . A similar trend of L_i growth results at both Reynolds numbers: the steepest increase happens when $\alpha = 24$ – 26 deg. However, if the boundary-layer thickness δ is used for nondimensionalization, the difference of L_i/δ is about 3 between the 20 deg ramp SWBLIs at Re_1 and Re_2 , but it shrinks for steeper ramps. It should be pointed out that the L_i/δ at Re_1 and Re_2 are very close at the 28 and 30 deg ramps, suggesting that the boundary-layer thickness could be a more appropriate scaling parameter for the interaction length when the ramp angle is larger than the largest flow deflection angle according to the inviscid oblique shock relation.

Different from the Re_1 cases, the reattachment shock wave at Re_2 is visible in all the ramps. Moreover, the separation shock and reattachment shock do not coalesce in the present field of view. In another experimental visualization on the SWBLI at a 28 deg

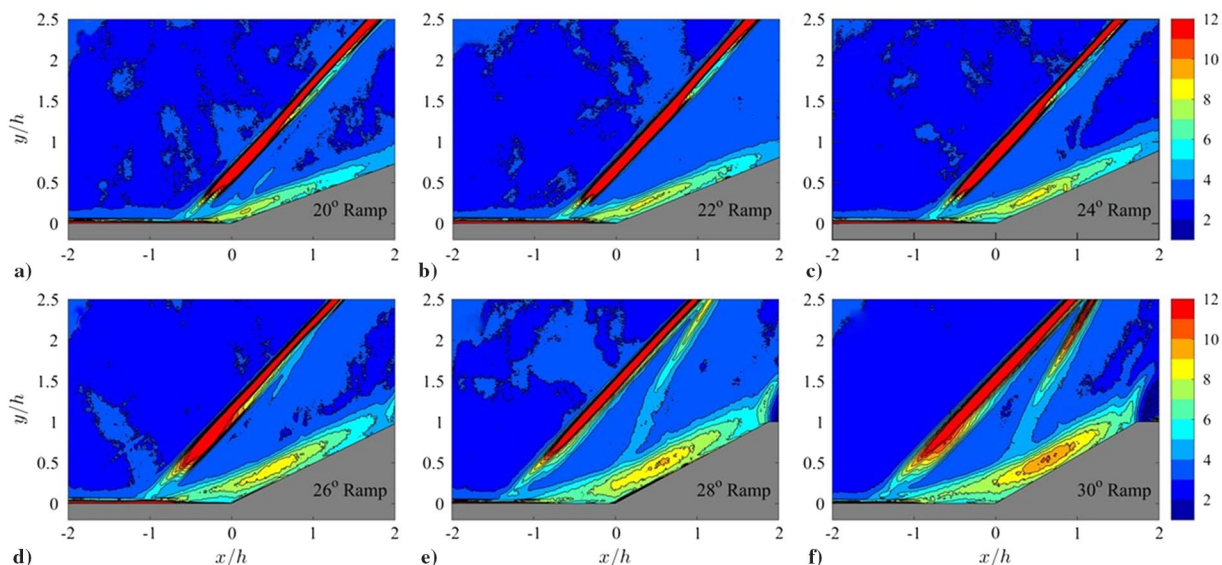


Fig. 4 Contours of I_{RMS} for SWBLIs at Re_1 .

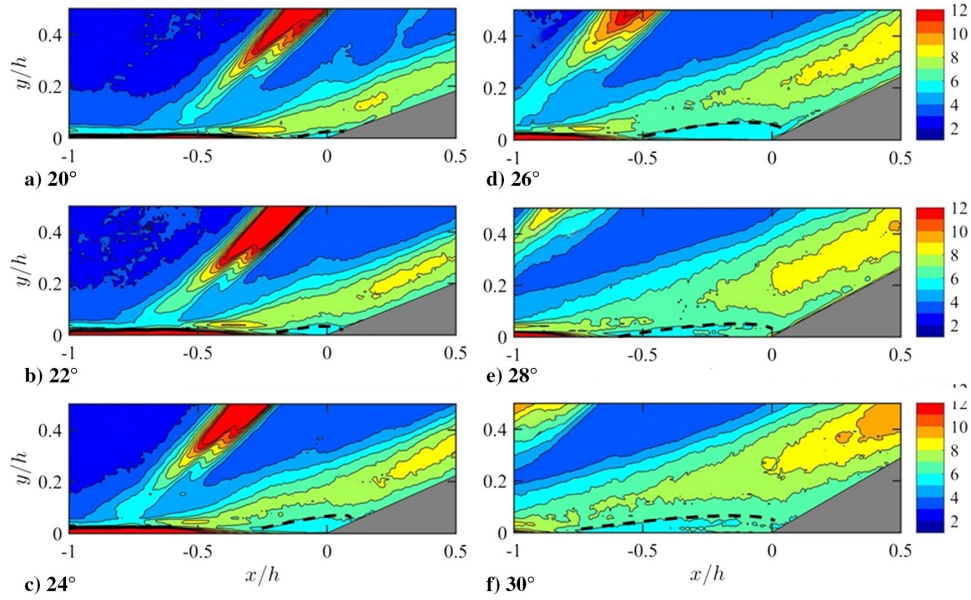


Fig. 5 Close-up view on the I_{RMS} contour at the ramp corner at Re_1 . Dashed lines indicate the boundary of the weak I_{RMS} region at the ramp corner.

compression ramp at $Ma = 3.0$ and $Re_\delta = 76,500$ [16], a similar shock-wave pattern was visualized, where separation and reattachment shock waves did not merge. The aforementioned discussion proves that the boundary-layer thickness δ is an underpinning parameter for the shock-wave structure.

The contour of I_{RMS} for SWBLIs at Re_2 are shown in Fig. 8. The SWBLIs at Re_2 , in general, result in a stronger I_{RMS} magnitude over the ramp than their counterparts at Re_1 . The separation and reattachment shock waves are represented by the high concentration of I_{RMS} in each SWBLI at Re_2 . In contrast, the reattachment shock wave have much weaker I_{RMS} intensity at Re_1 . Moreover, the

thickness of both the interaction region and the turbulent region over the ramp at Re_2 are also significantly larger. The peak I_{RMS} for the 20 deg ramp at Re_2 is more than 10 counts. It seems the increase of peak I_{RMS} is not monotonic. The I_{RMS} over the 28 deg ramp has a peak magnitude over 13 counts, whereas that of the 30 deg ramp decreases slightly to 12 counts. The location of peak I_{RMS} moves downstream along the ramp from $x/h = 0.1$ to 0.6 at Re_1 . Differently, it does not exhibit a large streamwise movement at Re_2 .

The corner region of lower I_{RMS} magnitude observed in SWBLIs at Re_1 was conjectured in association with the separation bubble. A similar region of weaker I_{RMS} can be identified in SWBLIs when

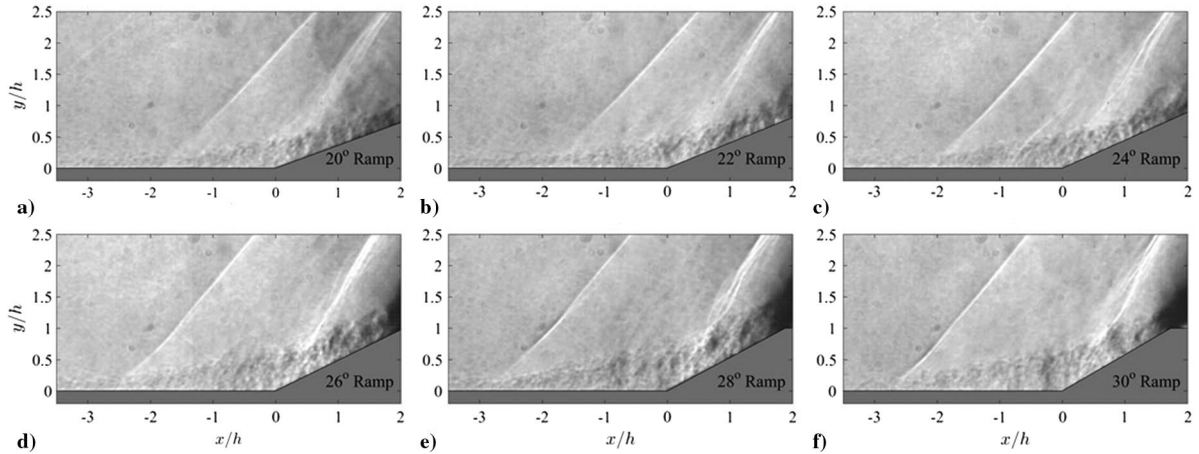


Fig. 6 Schlieren snapshots for SWBLIs at Re_2 .

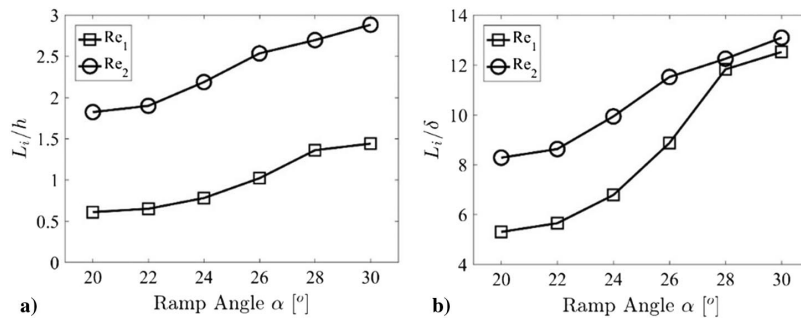


Fig. 7 Growth of interaction length L_i with ramp angle α at Re_1 and Re_2 : a) L_i scaled by h ; and b) L_i scaled by δ .

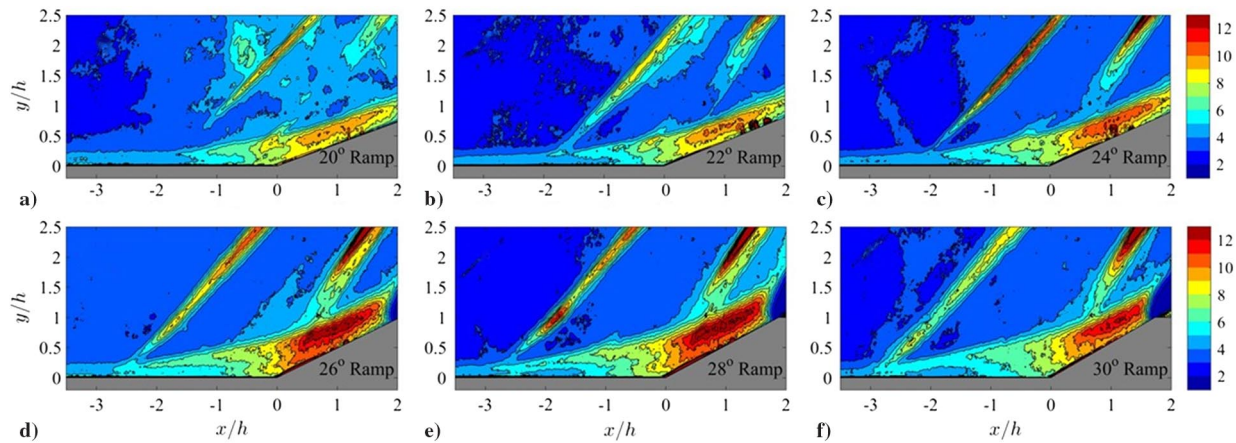


Fig. 8 Contours of I_{RMS} for SWBLIs at Re_2 .

$\alpha = 28$ and 30 deg in Fig. 8. Instead of appearing right at the ramp corner, it is located within the range of $x/h = -2.5 \sim -1.4$ for the 28 deg ramp and within the range $x/h = -2.5 \sim -1.2$ for the 30 deg ramp. But, in the SWBLIs at the other smaller ramps, this region of weaker I_{RMS} does not show up as a closed region and is open at its leading edge. It becomes partially closed in the 26 deg ramp. This gradual change of the low I_{RMS} region probably suggests the formation of the shock-induced flow separation with the increase of ramp angle, but further evidence through velocity measurements is needed.

So far, the flow organization and the fluctuation in the SWBLIs at six ramp angles and two different Reynolds numbers have been discussed. In the next section, the unsteady motion of the shock waves will be analyzed through a spectral analysis.

C. Shock-Wave Unsteadiness

The schlieren images are used as an optical sensor to study the shock-wave oscillation. A shock-wave detection algorithm is developed, where the shock-wave position is identified through the maximum gradient of the schlieren intensity across the streamwise direction. Because the entire ensemble is used, the resulting temporal sequence of shock-wave position contains 10,000 points and 9000 points for Re_1 and Re_2 cases, respectively. In an earlier experimental study on the unsteady shock wave induced by a vertical cylinder [17], the shock wave was detected in the high-speed schlieren images recorded at 100 kHz, and the shock-wave motion was verified by pressure sensors. This imaged-based technique was further employed to study the shock-wave unsteadiness in a transitional boundary-layer and shock-wave interaction [18]. In the present study, the shock waves at the height of $y/h = 1.5$ are investigated because the separation and reattachment shock waves are strong and clear at this height in both Reynolds number cases. The standard fast Fourier transformation (FFT) is applied to retrieve the spectrum of the shock-

wave unsteadiness. Since 2^{13} points are used in the FFT operation, the resulting frequency resolution is 2.44 Hz.

The premultiplied spectra $f \cdot P(f)$ of the separation shock in SWBLIs at Re_1 are organized into a contour plot in Fig. 9 so that spectral variation in relation to the ramp angle can be studied. Increased spectral intensity can be observed in the frequency band of 100 – 1000 Hz, and it centers at about 600 Hz ($St_\delta = 0.0026$), which agrees with the established knowledge of low-frequency unsteadiness. The peak spectral intensity for the low-frequency unsteadiness becomes stronger under a larger ramp angle. It should be mentioned that the narrow peak at 22 Hz in all the ramps is associated with the model vibration, which is due to the model's vertical cantilever-type installation.

The reattachment shock can be faithfully detected only when the ramp angle is larger than 28 deg at Re_1 . The premultiplied spectrum of the reattachment shock for the 28 deg ramp is shown in Fig. 10a as an example, where that of the separation shock is also included for comparison. It should be noted that the spectra shown in Fig. 10 are processed through the Welch method using blocks of 512 samples and the Hamming window function with 50% overlap. This operation is employed to filter out the random noise in the original spectra shown in Fig. 9 but at the expense of a reduced frequency resolution, namely, a frequency resolution of 39 Hz. According to Fig. 10a, the reattachment shock wave also exhibits intensified magnitude in the low-frequency band. The peak magnitude of the reattachment shock happens at 820 Hz ($St_\delta = 0.0037$), which is slightly larger than that of the separation shock, for which the peak is at 660 Hz ($St_\delta = 0.0030$). Sartor et al. [19] studied the unsteady shock wave in a transonic SWBLI on a baseline shock generation bump. It revealed that the reattachment shock-wave motion was closely correlated with the

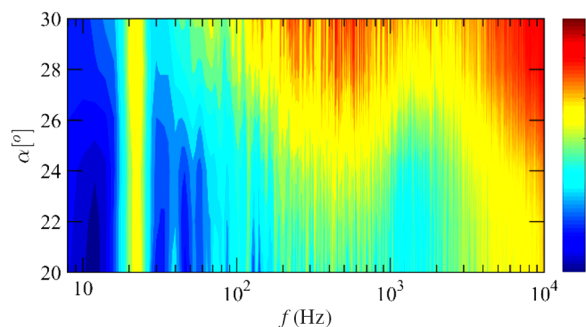


Fig. 9 Premultiplied spectra $f \cdot P(f)$ (in units of millimeters per second) of the separation shock-wave oscillations at $y/h = 1.5$ in SWBLIs at Re_1 .

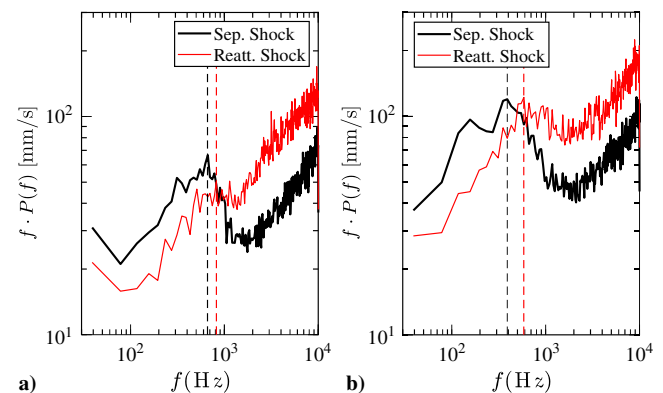


Fig. 10 Premultiplied spectra of separation (Sep.) and reattachment (Reatt.) shock waves in 28 deg ramp SWBLIs at a) Re_1 and b) Re_2 . Vertical dashed lines are the central frequency of the low-frequency unsteadiness of both shock waves.

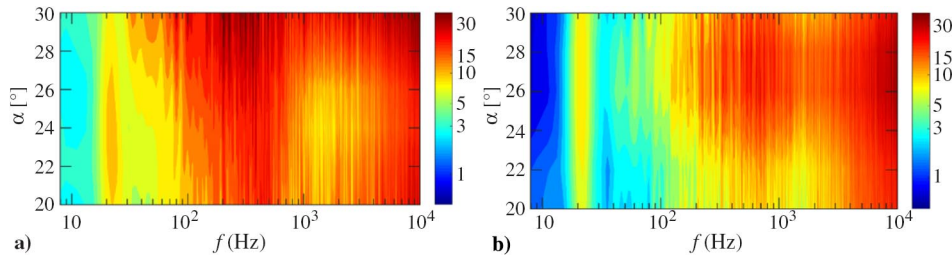


Fig. 11 Premultiplied spectra $f \cdot P(f)$ (in units of millimeters per second) of the a) separation and b) reattachment shock-wave oscillations at $y/h = 1.5$ in SWBLIs at Re_2 .

vortical activity in the separated shear layer where the reattachment shock originated. Similarly, the reattachment shock frequency in the present SWBLI should also indicate the characteristic frequency of the vortex shedding activity in the separated shear layer over the compression ramp.

The premultiplied spectral contours for both shock waves at Re_2 are shown in Fig. 11. Not surprisingly, the contour of separation shock spectra has the low-frequency unsteadiness, for which the intensity also increases with the ramp angle. However, the peak of present low-frequency unsteadiness appears at around 400 Hz, which is smaller than that at Re_1 . To better appreciate the Reynolds number effect on the shock-wave unsteadiness, the separation shock spectra in the 28 deg ramp SWBLIs at both Reynolds numbers are compared in Fig. 12a. Despite the broadband feature across the low-frequency domain, the separation shock spectrum at Re_2 exhibits stronger magnitudes, whereas its peak frequency shifts toward a lower frequency around 390 Hz, which is smaller than that of the separation shock at Re_1 .

The spectral contour of the reattachment shock at Re_2 is shown in Fig. 11b. Similar to the separation shock, the reattachment shock's intensity of low-frequency unsteadiness increases with ramp angle. However, it seems that a slight decrease in intensity happens in the 30 deg ramp spectrum. A closer comparison between the two spectral contours in Fig. 11 reveals that the peak frequency for both shock waves at Re_2 becomes smaller than that at Re_1 . This observation is further supported by the shock-wave spectra in the 28 deg ramp SWBLI at Re_2 ; see Fig. 10b. The peak frequencies of the separation shock and reattachment shock reduce to 390 and 585 Hz, respectively, which are smaller than their counterparts at Re_1 .

The Reynolds number effect on the reattachment shock is finally explored through the shock-wave spectra over the 28 deg ramp; see Fig. 12b. As revealed earlier, although the peak frequency shifted from 820 to 585 Hz when the Reynolds number increased from Re_1 to Re_2 , this change in peak frequency is less than that of the separation shock. Hence, the Reynolds number effect on spectrum modulation is weaker for the reattachment shock wave.

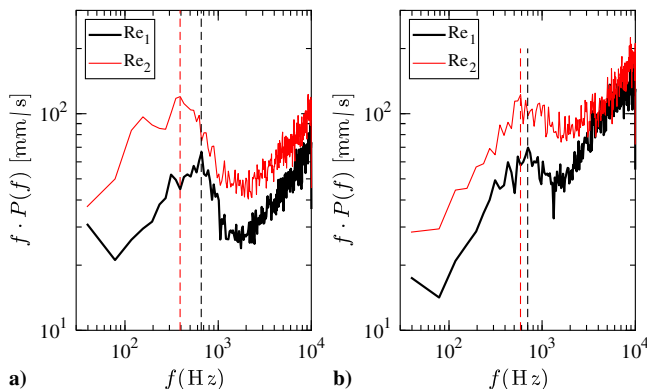


Fig. 12 Premultiplied spectra $f \cdot P(f)$ (in units of millimeters per second) of the a) separation and b) reattachment shock-wave oscillations at $y/h = 1.5$ in the 28 deg ramp SWBLIs at Re_1 and Re_2 .

IV. Conclusions

Through the present experimental investigation on SWBLIs at compression ramps, the high-speed schlieren has been demonstrated as a powerful tool in examining the SWBLI flow organization and unsteadiness. The converged RMS schlieren intensity I_{RMS} enables visualization of flow structures that are not immediately available in the raw schlieren snapshot, such as the peak turbulent region over the ramp surface and the region of weaker I_{RMS} at the ramp corner. The latter was conjectured as a representation of the separation bubble, but further validation is needed.

The effects of the ramp angle and Reynolds number on the compression ramp SWBLI have been examined. The interaction strength was varied by using ramps with angles between 20 and 30 deg. The interaction length grew with the ramp angle, whereas the steepest increase took place in the 24 and 26 deg ramps. Moreover, a steeper ramp resulted in a stronger interaction, namely, a thicker turbulent region and a stronger I_{RMS} magnitude. The Reynolds number was changed by increasing the thickness of the incoming turbulent boundary layer. The structure of the SWBLI was altered significantly by increasing the Reynolds number. The interaction region became longer, and the turbulent region over the ramp surface was stronger. Most of all, the reattachment shock appeared in all the SWBLIs at Re_2 , whereas it could only be clearly observed over the 28 and 30 deg ramps at Re_1 .

The shock-wave unsteadiness was examined in the end. The typical low-frequency oscillation was clearly revealed in the shock-wave spectra. A larger ramp angle gave rise to a stronger spectral intensity in the low-frequency band. The Reynolds number or the thickness of turbulent boundary layer affected the shock wave's unsteadiness. The SWBLI under the same ramp at Re_2 obtained stronger spectral intensity in the low-frequency band. Moreover, the Reynolds number was effective in frequency modulation. The larger Reynolds number resulted in a lower peak frequency for both separation and reattachment shock waves. In the present experiment, the reduction in peak frequency was 270 and 235 Hz for the separation shock and reattachment shock, respectively.

The present experimental work using high-speed schlieren with a short exposure time provides fundamental understanding of the compression ramp SWBLIs and creates the foundation for future experiments using other quantitative measurement techniques, such as particle image velocimetry, through which some of the observations and the associated conjectures can be further quantified and confirmed.

Acknowledgments

This research is supported by the U.K. Royal Society (RSG\R1\180236), the U.K. Engineering Physical Sciences Research Council (EP/R013608/1), and the Natural Science Foundation of China (51522606, 11902360).

References

- [1] Dolling, D. S., "Fifty Years of Shock-Wave/Boundary-Layer Interaction Research: What Next?" *AIAA Journal*, Vol. 39, No. 8, 2001, pp. 1517–1531. <https://doi.org/10.2514/2.1476>

- [2] Priebe, S., and Pino Martin, M., "Low-Frequency Unsteadiness in Shock Wave-Turbulent Boundary Layer Interaction," *Journal of Fluid Mechanics*, Vol. 699, May 2012, pp. 1–49.
<https://doi.org/10.1017/jfm.2011.560>
- [3] Pasquarile, V., Hickel, S., and Adams, N. A., "Unsteady Effects of Strong Shock-Wave/Boundary-Layer Interaction at High Reynolds Number," *Journal of Fluid Mechanics*, Vol. 823, July 2017, pp. 617–657.
<https://doi.org/10.1017/jfm.2017.308>
- [4] Gaitonde, D. V., "Progress in Shock Wave/Boundary Layer Interactions," *Progress in Aerospace Science*, Vol. 72, Jan. 2015, pp. 80–99.
<https://doi.org/10.1016/j.paerosci.2014.09.002>
- [5] Chang, J., Li, N., Xu, K., Bao, W., and Xu, D., "Recent Research Progress on Unstart Mechanism, Detection and Control of Hypersonic Inlet," *Progress in Aerospace Science*, Vol. 89, Feb. 2017, pp. 1–22.
<https://doi.org/10.1016/j.paerosci.2016.12.001>
- [6] Babinsky, H., and Harvey, J. K., *Shock Wave-Boundary-Layer Interactions*, 1st ed., Cambridge Univ. Press, New York, 2012.
- [7] Zheltovodov, A. A., "Shock Waves/Turbulent Boundary-Layer Interactions—Fundamental Studies and Applications," AIAA Paper 1996-1977, 1996.
- [8] Loginov, M. S., Adams, N. A., and Zheltovodov, A. A., "Large-Eddy Simulation of Shock-Wave/Turbulent-Boundary-Layer Interaction," *Journal of Fluid Mechanics*, Vol. 565, Oct. 2006, pp. 135–169.
<https://doi.org/10.1017/S0022112006000930>
- [9] Muzio, G., Peter, F., Hickel, S., and Adams, N. A., "Large-Eddy Simulation of a Supersonic Turbulent Boundary Layer over a Compression-Expansion Ramp," *International Journal of Heat and Fluid Flow*, Vol. 42, Aug. 2013, pp. 79–93.
<https://doi.org/10.1016/j.ijheatfluidflow.2012.12.006>
- [10] Dupont, P., Haddad, C., and Debieve, J. F., "Space and Time Organization in a Shock-Induced Separated Boundary Layer," *Journal of Fluid Mechanics*, Vol. 559, July 2006, pp. 255–277.
<https://doi.org/10.1017/S0022112006000267>
- [11] Clemens, N. T., and Narayanaswamy, V., "Low-Frequency Unsteadiness of Shock Wave/Turbulent Boundary Layer Interactions," *Annual Review of Fluid Mechanics*, Vol. 46, No. 1, 2014, pp. 469–492.
<https://doi.org/10.1146/annurev-fluid-010313-141346>
- [12] Grilli, M., Schmid, P. J., Hickel, S., and Adams, N. A., "Analysis of Unsteady Behaviour in Shockwave Turbulent Boundary Layer Interaction," *Journal of Fluid Mechanics*, Vol. 700, No. 8, 2012, pp. 16–28.
<https://doi.org/10.1017/jfm.2012.37>
- [13] Laurence, S. J., Wagner, A., and Hannemann, K., "Schlieren-Based Techniques for Investigating Instability Development and Transition in a Hypersonic Boundary Layer," *Experiments in Fluids*, Vol. 55, Aug. 2014, Paper 1782.
<https://doi.org/10.1007/s00348-014-1782-9>
- [14] Combs, C. S., Schmisser, J. D., Bathel, B. F., and Jones, S. B., "Unsteady Analysis of Shock-Wave/Boundary-Layer Interaction Experiments at Mach 4.2," *AIAA Journal*, Vol. 57, No. 11, Nov. 2019.
<https://doi.org/10.2514/1.j058073>
- [15] Verma, S. B., Manisankar, C., and Raju, C., "Control of Shock Unsteadiness in Shock Boundary-Layer Interaction on a Compression Corner Using Mechanical Vortex Generators," *Shock Waves*, Vol. 22, No. 4, 2012, pp. 327–339.
<https://doi.org/10.1007/s00193-012-0369-8>
- [16] Wu, Y., Yi, S., He, L., and Chen, Z., "Flow Visualization of Mach 3 Compression Ramp with Different Upstream Boundary Layers," *Journal of Visualization*, Vol. 18, No. 4, 2015, pp. 631–644.
<https://doi.org/10.1007/s12650-014-0255-9>
- [17] Combs, C. S., Kreth, P. A., Schmisser, J. D., and Lara Lash, E., "Image-Based Analysis of Shock-Wave/Boundary Layer Interaction Unsteadiness," *AIAA Journal*, Vol. 56, No. 3, 2018, pp. 1288–1293.
<https://doi.org/10.2514/1.J056390>
- [18] Combs, C. S., Lara Lash, E., Kreth, P. A., and Schmisser, J. D., "Investigating Unsteady Dynamics of Cylinder-Induced Shock-Wave/Transitional Boundary-Layer Interactions," *AIAA Journal*, Vol. 56, No. 4, 2018, pp. 1588–1599.
<https://doi.org/10.2514/1.J056553>
- [19] Sartor, F., Mettot, C., Bur, R., and Sipp, D., "Unsteadiness in Transonic Shock-Wave/Boundary Layer Interactions: Experimental Investigations and Global Stability Analysis," *Journal of Fluid Mechanics*, Vol. 781, Oct. 2015, pp. 550–577.
<https://doi.org/10.1017/jfm.2015.510>

R. D. Bowersox
Associate Editor